Published in final edited form as:
Neuroimage. 2012 January 16; 59(2): 979–985. doi:10.1016/j.neuroimage.2011.08.064.

In vivo quantification of T2* anisotropy in white matter fibers in marmoset monkeys

P. Sati[1], **A. C. Silva**[2], **P. van Gelderen**[3], **M. I. Gaitan**[1], **J. E. Wohler**[4], **S. Jacobson**[4], **J. H. Duyn**[3], and **D. S. Reich**[1]

[1]Translational Neuroradiology Unit, Neuroimmunology Branch, National Institute of Neurological Disorders and Stroke, National Institutes of Health, Bethesda, Maryland, USA

[2]Cerebral Microcirculation Unit, Laboratory of Functional and Molecular Imaging, National Institute of Neurological Disorders and Stroke, National Institutes of Health, Bethesda, Maryland, USA

[3]Advanced MRI Section, Laboratory of Functional and Molecular Imaging, National Institute of Neurological Disorders and Stroke, National Institutes of Health, Bethesda, Maryland, USA

[4]Viral Immunology Section, Neuroimmunology Branch, National Institute of Neurological Disorders and Stroke, National Institutes of Health, Bethesda, Maryland, USA

Abstract

T_2^*-weighted MRI at high field is a promising approach for studying noninvasively the tissue structure and composition of the brain. However, the biophysical origin of T_2^* contrast, especially in white matter, remains poorly understood. Recent work has shown that R_2^* (=1/T_2^*) may depend on the tissue's orientation relative to the static magnetic field (B_0) and suggested that this dependence could be attributed to local anisotropy in the magnetic properties of brain tissue. In the present work, we analyzed high-resolution, multi-gradient-echo images of in vivo marmoset brains at 7T, and compared them with ex vivo diffusion tensor images, to show that R_2^* relaxation in white matter is highly sensitive to the fiber orientation relative to the main field. We directly demonstrate this orientation dependence by performing in vivo multi-gradient-echo acquisitions in two orthogonal brain positions, uncovering a nearly 50% change in the R_2^*relaxation rate constant of the optic radiations. We attribute this substantial R_2^* anisotropy to local subvoxel susceptibility effects arising from the highly ordered and anisotropic structure of the myelin sheath.

Keywords

Anisotropic R_2^* relaxation rate; white matter fiber orientation; myelin; high-field imaging; nonhuman primate brain

Corresponding author: Dr. Pascal Sati, Translational Neuroradiology Unit, Neuroimmunology Branch, National Institute of Neurological Disorders and Stroke, National Institutes of Health, 9000 Rockville Pike, Building 10/5C205, Bethesda, MD 20892-1584, Phone#: 301-594-7217, Fax#: 301-402-0373, satip@ninds.nih.gov.

Introduction

Magnetic susceptibility contrast obtained with gradient echo (GRE) MRI techniques offers unique opportunities to study the human brain. At clinical field strengths of 3T and below, this contrast has been used intensively to study neuronal activation (Ogawa et al., 1990), image the venous vasculature (Reichenbach et al., 1997), and detect hemorrhagic infarcts (Scharf et al., 1994). In addition, susceptibility contrast may reflect tissue iron (Haacke et al., 2005) and myelin content (Hwang et al., 2010), and it may also be applied to evaluate tissue integrity in neuroimmunological diseases (Sati et al., 2010). At higher field strength (above 3T), GRE techniques are extremely promising due to the increase in contrast and resolution that facilitates the study of fine anatomical details within gray and white matter (WM) (Duyn et al., 2007; Li et al., 2006). Although primarily attributed to magnetic susceptibility variations, the origin of GRE contrast remains poorly understood, which hampers its widespread application especially in clinical settings.

An interesting recent finding is that in WM, the time constant of T_2^* decay and consequently the GRE signal amplitude may depend on the tissue's orientation relative to the static magnetic field (B_0) (Bender and Klose, 2010; Cherubini et al., 2009; Denk et al., 2011; Lee et al., 2011a; Schäfer et al., 2009; Wiggins et al., 2008). This orientation dependence has been attributed to anisotropic magnetic properties on the subvoxel scale, including susceptibility anisotropy (Lee et al., 2010; Lee et al., 2011a; Liu, 2010) and anisotropic tissue compartmentalization (He and Yablonskiy, 2009; Yablonskiy and Haacke, 1994). Therefore, quantifying the orientation dependence of T_2^* may provide new information about the mechanisms underlying GRE contrast and consequently about subvoxel tissue structures that could be altered by disease.

So far, quantification of the orientation dependence of T_2^* contrast has been challenging due to the difficulty of rotating a subject's head in the MRI system, leading some researchers to study postmortem tissue samples (Lee et al., 2010; Lee et al., 2011a). However, postmortem samples may be affected by changes in water compartmentalization due to cell swelling and other structural and molecular changes that may affect T_2^* relaxation. To overcome this issue, in this work we investigated the orientation effects on R_2^* ($=1/T_2^*$) relaxation rate in the common marmoset.

The common marmoset (*Callithrix jacchus*) is a small New World nonhuman primate of growing importance for research in neuroscience. The marmoset has a lissencephalic brain with a similar anatomical organization to the brains of other primates, including humans. Moreover, the gray-to-WM volume ratio of the marmoset brain is close to that of the human. MRI has been increasingly used to study its brain structure (Bock et al., 2009; Yamada et al., 2008) and function (Brevard et al., 2006; Ferris et al., 2001) as well as brain tissue alterations caused by various diseases (Bihel et al., 2010; Kap et al., 2010), and combined histological and MRI brain atlases of the marmoset have become available (Hikishima et al., 2011; Newman et al., 2009). T_1 relaxometry of gray and white matter of the marmoset brain has also been reported (Liu et al., 2011b). In addition, because the marmoset is small with respect to the magnet bore size, its head can be easily rotated in vivo inside the bore so that the effects of tissue orientation can be accurately probed. Therefore, this nonhuman primate appears to be an excellent in vivo model system for addressing basic questions about the origin of the MRI T_2^* contrast.

Based on these considerations, we hypothesized that the application of GRE imaging in marmoset brain at 7T could enable quantification and improved interpretation of T_2^* anisotropy at high fields while providing new detailed anatomical information about this small nonhuman primate brain. In this study, we focused our attention on the in vivo

quantification of the orientation dependence of R_2^* relaxation rate, informing our results with an ex vivo diffusion tensor imaging (DTI) experiment to identify the main WM fiber bundles and their directions within the marmoset brain.

Material and Methods

The NINDS/NIDCD Animal Care and Use Committee approved all experiments. Experiments were carried out in 5 common marmosets aged 3.6 ± 0.4 years (mean ± standard deviation) and weighting 416 ± 32 g. Marmosets were housed two to a cage with a 12h light/dark cycle on an ad libitum diet of Zupreem canned marmoset food, Purina 5040 biscuits, unfiltered water, P.R.A.N.G. rehydrator, and fruit and vegetable treats.

On the day of each MRI experiment, the animals were fasted for 12h, retrieved from their cage, and transported to the MRI lab. The animals were sedated with an intramuscular injection of 10 mg/kg ketamine, orally intubated, and mechanically ventilated with a mixture of medical air and oxygen. Anesthesia was maintained with isoflurane at a typical concentration of 2%. Following preparation, the animals were placed on an MRI compatible cradle, and their heads were fixed to a custom-made stereotaxic frame using nonpiercing earpieces, which were placed in the ear canals after application of 2% lidocaine as a topical analgesic. Throughout the MRI session, physiological parameters including end-tidal CO_2, heart rate, and SPO_2 were continuously monitored using a capnograph and pulse oximeter (Surgivet, Waukesha, WI, USA). Rectal temperature was continuously monitored and maintained at 38.5 °C with a water heating pad.

MRI was performed on a 7T/30 cm USR/AVIII MRI scanner (Bruker-Biospin Corp., Ettlingen, Germany) equipped with a 15 cm gradient set of 450 mT/m strength (Resonance Research Inc., Billerica, MA, USA). A custom-built, 16-rung, high-pass birdcage radiofrequency coil with a 12 cm inner diameter was used for transmission and a custom-built five-element receive-only phased array equipped with preamplifiers was used for reception. Three monkeys were scanned using a routine imaging protocol that included various sequences. During this routine session, the marmosets were positioned in the magnet bore with the body in prone position and the head looking out to the service end of magnet (sphinx position). The elements of the receiver phased array were arranged to cover the whole brain and were placed directly on top of the head (approximately centered over the parietal cortex). For the other two monkeys, a different imaging protocol dedicated to the head rotation experiment was performed. In this protocol, the monkeys were first imaged in the sphinx position, similar to the routine protocol. Then, during the same session, the monkeys were imaged with the body in supine position and the head looking up perpendicularly to the main field (supine position). In this position, the phased array was placed at the back of the brain (approximately centered over the occipital cortex).

For all the marmosets, the MRI protocol included a T_2-weighted spin-echo three-plane localizer, a 3D B_0 field mapping sequence followed by first and second-order localized shimming, and a 2D multi-gradient-echo (MGRE) sequence. For the MGRE sequence, 40 slices were acquired with an in-plane resolution of 150 × 150 μm^2 and slice thickness of 600 μm (FOV = 38.4 mm × 38.4 mm × 24 mm and matrix = 256 × 256 × 40). Six echoes (TE = 3.5, 10.5, 17.5, 24.5, 31.5, and 38.5 ms) were collected using flyback for positive GRE readout. Other parameters were: repetition time = 2500 ms, flip angle = 90°, number of averages = 1. Acquisition time for the MGRE sequence was 10 min 40 s. For one monkey, the number of averages (NEX) was increased to 4 in both sphinx and supine positions. The acquired MGRE datasets were then collected for offline processing using Matlab (MathWorks, Inc.).

Because the voxels were anisotropic (the voxel dimension in the slice-select direction was four times larger than the in-plane voxel dimensions), the slice-select direction was particularly sensitive to background magnetic fields, which can compromise the measurement of T_2^*. Therefore, the effect of these background fields along the slice-select direction was estimated at each voxel and corrected assuming a sinc function (Yablonskiy, 1998). The corrected magnitude signal intensities from all echoes were then fitted to a single exponential decay, and T_2^* maps were generated by running this fitting procedure separately for all voxels. Regions of interest (ROIs) were drawn manually on T_2^*-weighted images, and mean R_2^* relaxation rate with associated standard deviation was calculated in each ROI.

The ex vivo study was conducted in the same magnet using a formalin-fixed brain from a sacrificed healthy female monkey (age = 4 years, weight = 350 g). The use of ex vivo tissue was motivated by the need for long scan times to achieve high spatial resolution for resolving the WM fiber architecture of the monkey brain as well as an excellent signal-to-noise ratio for accurate assessment of the individual fiber directions. The brain was placed in a plastic tube filled with Fomblin (Ausimont USA, Thorofare NJ) and inserted into a volume transmit-receive RF coil with 40 mm diameter (Bruker-Biospin). After running a localizer and first and second-order B_0 correction procedure, a high-resolution (150 μm^3 isotropic) DTI experiment was performed using a spin-echo sequence with a segmented EPI readout. The acquisition without diffusion weighting (b-value = 0 s/mm^2) was repeated 6 times, whereas each of the 30 noncollinear directions with b-value = 4000 s/mm^2 was acquired once. The other parameters of this sequence were: TE = 41 ms, TR = 700 ms, FOV = 38.4 mm × 28.8 mm × 32.7 mm, matrix = 256 × 192 × 218, number of segments = 12. Total acquisition time for the DTI experiment was ~36 hours. DTI data were processed using a home-built automated pipeline running under MIPAV software (Medical Image Processing, Analysis & Visualization, NIH) using JIST (Java Image Science Toolkit, Vanderbilt University) (Lucas et al., 2010). Fractional anisotropy (FA) maps and color-encoded FA maps were generated. ROIs corresponding to different fiber bundles were drawn manually on FA maps, and the mean FA value with its associated standard deviation was calculated in each ROI. For the color-encoded FA maps, principal colors (red, green, and blue) were assigned to each axis of reference on the magnet, with red indicating the right-left axis; green, the anteroposterior axis; and blue, the rostrocaudal axis.

Finally, images of whole mount sections stained for myelin coming, taken from an online atlas of the marmoset (http://udn.nichd.nih.gov/aboutatlas.html), were used for comparison with MRI images. The correspondence between postmortem and MRI images was made visually using structural brain landmarks.

Results

Fig. 1 shows the high-resolution color-encoded fractional anisotropy (FA) maps of the formalin-fixed marmoset brain. The major WM fibers are identified, including the anterior commissure (AC), genu (GCC), and splenium (SCC) of the corpus callosum; corticospinal tracts (CST); optic tracts (OT); and optic radiations (OR). These fibers display high FA values ($FA_{AC} \approx FA_{GCC} \approx FA_{SCC} = 0.7 \pm 0.1$ [mean ± SD] and $FA_{OR} = 0.6 \pm 0.1$) relative to cortical gray matter, which has an average FA value of 0.2 ± 0.1. Therefore, the WM structures in marmoset brain appear to be highly organized. Interestingly, the posterior part of the cerebral WM shows adjacent bundles (the OR in green and surrounding fibers in red-purple) that are mutually orthogonal. Note also that some cortical areas show mild diffusion anisotropy with a preferred orientation normal to the cortical surface (red color).

In vivo imaging was generally performed when the marmoset was placed in sphinx position (see localizer on left of Fig. 2). Additionally, in two monkeys, the acquisition was repeated

during the same scanning session using the supine position (see localizer on right of Fig. 2). High-quality images were acquired in both brain positions, but due to coil positioning, better brain volume coverage was achieved in the sphinx position.

Fig. 3 shows typical coronal slices with T_2^* weighting (images on left) acquired in the sphinx position. To increase the signal-to-noise ratio while maintaining good tissue contrast, these images were generated by averaging the three last magnitude echoes (TE = 24.5, 31.5, and 38.5 ms), which are heavily T_2^*-weighted. Throughout the brain, there is a clear delineation between gray matter, WM, and cerebrospinal fluid, indicating that excellent tissue contrast can be achieved with T_2^* contrast. Such contrast also allows identification of the major WM fibers, in which R_2^* relaxation rates are evaluated (below). Details of the microvasculature across the cortical ribbon can be observed due to signal loss (dephasing) within veins. There is also a substantial contrast variation within the substance of the WM, especially in the posterior part of brain. Apart from these tissue-specific intensity variations, non-tissue-specific intensity variations are observed in the inferior temporal lobes. These are due to incompletely removed macroscopic magnetic field inhomogeneities caused by the tissue-air interfaces in the paranasal sinuses.

All of the previously described features observed in the T_2^*-weighted images were also observed in the quantitative R_2^* maps (images on right in Fig 3). Calculated R_2^* values for different ROIs (Table 1) indicate that R_2^* values in the brain were in the range of 25 to 45 s^{-1}. Within WM, there was a heterogeneous distribution of R_2^* values. The GCC and SCC, which appear strongly hypointense on T_2^*-weighted images in the sphinx position, have the highest R_2^* values. The anterior commissure (AC) and the WM tracts that form the bright layers interfacing with the cortex in both cerebral hemispheres, designated WM1, also have relatively high R_2^* values. On the other hand, the region designated WM2, which is located deeper within the WM, has substantially lower R_2^* values. This R_2^* pattern was observed only when the animal was placed in the sphinx position. Note that some cortical gray matter areas (denoted mGM; see Fig. 4) have slightly higher R_2^* values than do neighboring cortical areas (denoted GM). As illustrated by the myelin-stained section (bottom image in Fig. 4), these R_2^* variations appear to correlate with the cortical myelination pattern.

Fig. 5 shows three different coronal slices of a monkey scanned in the two different positions (sphinx and supine). The R_2^* pattern described above was reproduced when this monkey was placed in the sphinx position (top row in Fig. 5). On the other hand, when the acquisition was repeated with the marmoset in the supine position, the R_2^* values changed drastically (middle row in Fig. 5). Specifically, R_2^* relaxation rates were decreased in region WM1 (see Table 2) but substantially increased in region WM2. Note that on the R_2^* maps acquired in supine position (middle row in Fig. 5), WM2 can be now clearly identified as the optic radiations (OR), which are readily observable in green color on the color-encoded FA maps (bottom row in Fig. 5). Finally, R_2^* relaxation rates for cortical gray matter (GM and mGM) did not change significantly when switching from sphinx to supine positioning.

Discussion and Conclusions

In this work, we present high-resolution T_2^*-weighted images of in vivo marmoset brains obtained at 7T. T_2^* contrast provided an excellent delineation of gray matter, WM, and cerebrospinal fluid, with a striking heterogeneous contrast within the WM of the posterior brain. These features were quantified by R_2^* ($1/T_2^*$) mapping, and a substantial variation of the R_2^* relaxation rate constant was measured across different WM fibers. Previous studies conducted in the human brain at the same field strength have reported similarly heterogeneous R_2^* relaxation rates in WM (Li et al., 2006; Li et al., 2009). However, the origin of this heterogeneity remains poorly understood. Interestingly, recent findings have

shown that the T_2^* amplitude and decay time constant of in vivo WM may depend on the orientation of the tissue relative to the static magnetic field (B_0) (Bender and Klose, 2010; Cherubini et al., 2009; Denk et al., 2011; Schäfer et al., 2009; Wiggins et al., 2008). In our study, we confirmed that fiber orientation indeed plays a major role in the generation of T_2^* contrast, and we quantified the in vivo effect of orientation on R_2^* relaxation at 7T.

After identifying the direction of different WM bundles inside the marmoset brain using high-resolution DTI (Fig. 1), we found that fibers oriented perpendicular to the B_0 field (AC, SCC, GCC and WM1 in sphinx; WM2, equivalent to the OR, in supine) have significantly higher R_2^* values ($\Delta R_2^* \approx 5$ –15 s^{-1}; Tables 1 and 2) than fibers oriented parallel to the B_0 field (WM2 in sphinx and WM1 in supine). Although differences in size and myelin content between these different fiber bundles might play a nonnegligible role in determining the R_2^* relaxation rate, by rotating the position of the marmoset brain, we provided direct evidence of the paramount effect of fiber orientation itself. Similar experiments using different head orientations have been previously performed in humans (Schäfer et al., 2009) and macaque monkeys (Wiggins et al., 2008), but the effect of head rotation has never been quantified in the same WM fibers. Here, we found that the optic radiations have the most striking anisotropic R_2^* relaxation rate constant with an average 50% increase ($\Delta R_2^* - 15\ s^{-1}$; Table 2) when the fibers were oriented perpendicularly to B_0 (supine position) relative to when they were oriented parallel to B_0 (sphinx position). Note that our findings are in excellent agreement with a similar in vivo experiment in humans at the same field strength (Wiggins et al., 2011).

These findings can be interpreted using the general description of the R_2^* relaxation rate constant as the combination of irreversible (R_2) and reversible (R_2') signal dephasing effects (with $R_2^* = R_2 + R_2'$). R_2 relaxation is caused by molecular-scale magnetic field variations that are governed by dipole-dipole interactions. Contrary to R_2', R_2 relaxation should not be sensitive to magnetic susceptibility effects and thus should be only minimally sensitive to orientation effects (i.e. R_2 is approximately isotropic).

However, obtaining an accurate measurement of R_2 is difficult, in part because R_2 measurements are sensitive to the effects of diffusion through local magnetic-field gradients, especially at high relaxation rate of white matter has been measured at 7T in fields and at the micron scale. The R_2 human brain [$R_2 \sim 21\ s^{-1}$] (Cox and Gowland, 2010), as well as in rat (Cremillieux et al., 1998) and mouse brain (Guilfoyle et al., 2003) [$R_2 \sim 28\ s^{-1}$]. Unfortunately, all of these experiments suffered from diffusion dephasing effects. For example, the choice of echo spacing for the multi-spin-echo experiment can significantly affect the measured T_2 times (Bartha et al., 2002; Stefanovic et al., 2003) by allowing non-negligible diffusion of spins through the tissue between pulses, which leads to signal loss that is not refocused using conventional spin-echo sequences. Therefore, these measured R_2 values may be considered to be upper bounds on the true R_2 relaxation rate. In order to obtain a realistic estimate of R_2' from our measured R_2^* values, we seek instead a lower bound on R_2. Field independence of the R_2 relaxation rate is expected on theoretical grounds (Bloembergen et al., 1948), and this is supported by measured R_2 values in human brain at lower field strengths ($R_2 \sim 10$–$15\ s^{-1}$ between 0.02T and 4T) (Agartz et al., 1991; Oros-Peusquens et al., 2008; Stanisz et al., 2005; Wansapura et al., 1999). Thus, the actual R_2 relaxation rate at 7T may also be as low as 10–15 s^{-1}. Based on our R_2^* measurements in different WM tracts (Table 1), the average R_2^* rate in marmoset brain is approximately 38 s^{-1}; using our lower bound estimate of R_2, this leads to R_2' in the range of 23–28 s^{-1}. This indicates that in WM at 7T, unlike at lower field strengths where R_2^* is significantly smaller (Gelman et al., 1999; Sati et al., 2010), the R_2' contribution to R_2^* may be substantial. This further indicates that the fractional orientation effect on R_2' ($\Delta R_2' = \Delta R_2^* \approx 15\ s^{-1}$ for the

optic radiations) is much stronger than that on R_2^* and likely exceeds 50% (that is, $\Delta R_2'/R_2'$ may be as high as 65%).

Some of the magnetic-field inhomogeneities that cause R_2' relaxation are on the macroscopic scale (i.e., they vary over distances larger than a single voxel) and are produced by magnetic susceptibility perturbations arising from sources including magnet imperfections and tissue-air interfaces such as the paranasal sinuses. In this work, most of these undesirable, non-tissue-specific effects were eliminated in WM areas using careful shimming and small voxel sizes and by applying a background magnetic-field correction along the slice-select direction. The remaining field inhomogeneities causing R_2' relaxation reflect local (subvoxel) susceptibility perturbations. In the brain, potential biological sources of magnetic susceptibility pertubers creating local and anisotropic field inhomogeneities on this scale include blood vessels containing deoxyhemoglobin (Yablonskiy, 1998), non-heme iron (Fukunaga et al., 2010), proteins and lipids in myelin sheets, and axonal structures (He and Yablonskiy, 2009; Lee et al., 2011a).

Based on our estimate of R_2' to be approximately 23–28 s^{-1}, the contribution from deoxygenated venous blood is unlikely to be the primary source of magnetic susceptibility in WM. Indeed, the R_2' relaxation created by deoxygenated blood has been evaluated in human WM to be on the order of 1 s^{-1} at 3T (He et al., 2008). Expecting linear dependence of R_2' on field strength, this translates to $R_2' \sim 2.3\ s^{-1}$ at 7T, significantly lower than our experimental estimate.

Although the non-heme iron has been suggested as a potentially important source of magnetic susceptibility affecting GRE signal at 7T in several brain regions (Fukunaga et al., 2010), it is not likely to explain the bulk of the orientation effects observed in white matter in this study. Whereas iron has been generally associated with the oligodendrocytes that are abundantly present in healthy white matter tracts (Connor and Menzies, 1996), the optic radiations are known to contain very little iron (Drayer et al., 1986). Therefore, in this fiber tract, and likely in others as well, other contributions must be responsible for much of the observed change in R_2' relaxation.

Because of the above arguments, it appears likely that a substantial contribution to R_2' in white matter originates from susceptibility effects caused by proteins or lipids in the highly ordered and anisotropic structures of myelin sheets and/or axons. There are some reasons to infer that the myelin sheets may actually be the dominant contributors. First, recent studies of fiber bundles with compromised myelin sheets in shiverer mice (Liu et al., 2011a) and cuprizone-fed mice (Lee et al., 2011b) have found an almost complete elimination of contrast in R_2^* and phase images. Second, the anisotropy of the magnetic susceptibility of cylindrical phospholipid bilayers has been demonstrated in vitro (Boroske and Helfrich, 1978). Finally, the sizes of anisotropic intra-axonal structures (axoplasmic reticulum tubules, neurofilaments, and microtubules in the cytoskeleton) are on the order of tens of nanometers, several orders of magnitude below the diffusion length of axonal water protons (a few micrometers) for the echo times used. Thus, strong diffusion averaging of these local fields will effectively minimize the R_2' contribution to R_2^*. We therefore attribute the substantial R_2^* anisotropy we have demonstrated here to the local subvoxel susceptibility effects generated by myelin sheets and suggest that R_2^* imaging represents a promising approach to assessing myelination, demyelination, and remyelination in vivo.

In conclusion, by analyzing high-resolution, MGRE images of in vivo marmoset brains at 7T as well as high-resolution, ex vivo diffusion tensor images, we have demonstrated that R_2^* relaxation in WM at 7T is highly sensitive to the fiber orientation relative to the main field. We directly demonstrated this orientation dependence by performing the in vivo

MGRE acquisition in two orthogonal brain positions, uncovering a nearly 50% change in the R_2^* relaxation rate constant of the same WM tract (the optic radiations). We interpreted this substantial R_2^* anisotropy as mainly caused by local subvoxel susceptibility effects generated by myelin and its highly ordered and anisotropic sheath structure.

Acknowledgments

We thank Dr. Hellmut Merkle for designing the 5-element receive coil used in this study, Dr. Frank Q. Ye for helping with the DTI acquisition, Colin D. Shea for support with MIPAV and JIST software, Xianfeng (Lisa) Zhang for animal preparation, and Dr. Luca Massacesi for insightful discussions. We also thank the Intramural Research Program of NINDS for support.

References

Agartz I, Saaf J, Wahlund LO, Wetterberg L. T1 and T2 relaxation time estimates in the normal human brain. Radiology. 1991; 181:537–543. [PubMed: 1924801]

Bartha R, Michaeli S, Merkle H, Adriany G, Andersen P, Chen W, Ugurbil K, Garwood M. In vivo 1H2O T2+ measurement in the human occipital lobe at 4T and 7T by Carr-Purcell MRI: detection of microscopic susceptibility contrast. Magn Reson Med. 2002; 47:742–750. [PubMed: 11948736]

Bender B, Klose U. The in vivo influence of white matter fiber orientation towards B(0) on T2* in the human brain. NMR Biomed. 2010; 23:1071–1076. [PubMed: 20665897]

Bihel E, Pro-Sistiaga P, Letourneur A, Toutain J, Saulnier R, Insausti R, Bernaudin M, Roussel S, Touzani O. Permanent or transient chronic ischemic stroke in the non-human primate: behavioral, neuroimaging, histological, and immunohistochemical investigations. J Cereb Blood Flow Metab. 2010; 30:273–285. [PubMed: 19794396]

Bloembergen N, Purcell EM, Pound RV. Relaxation Effects in Nuclear Magnetic Resonance Absorption. Physical Review. 1948; 73:679–712.

Bock NA, Kocharyan A, Liu JV, Silva AC. Visualizing the entire cortical myelination pattern in marmosets with magnetic resonance imaging. J Neurosci Methods. 2009; 185:15–22. [PubMed: 19737577]

Boroske E, Helfrich W. Magnetic anisotropy of egg lecithin membranes. Biophys J. 1978; 24:863–868. [PubMed: 367463]

Brevard ME, Meyer JS, Harder JA, Ferris CF. Imaging brain activity in conscious monkeys following oral MDMA (“ecstasy”). Magn Reson Imaging. 2006; 24:707–714. [PubMed: 16824965]

Cherubini A, Peran P, Hagberg GE, Varsi AE, Luccichenti G, Caltagirone C, Sabatini U, Spalletta G. Characterization of white matter fiber bundles with T2* relaxometry and diffusion tensor imaging. Magn Reson Med. 2009; 61:1066–1072. [PubMed: 19253372]

Connor JR, Menzies SL. Relationship of iron to oligodendrocytes and myelination. Glia. 1996; 17:83–93. [PubMed: 8776576]

Cox EF, Gowland PA. Simultaneous quantification of T2 and T’2 using a combined gradient echo-spin echo sequence at ultrahigh field. Magn Reson Med. 2010; 64:1440–1445. [PubMed: 20593370]

Cremillieux Y, Ding S, Dunn JF. High-resolution in vivo measurements of transverse relaxation times in rats at 7 Tesla. Magn Reson Med. 1998; 39:285–290. [PubMed: 9469712]

Denk C, Torres EH, Mackay A, Rauscher A. The influence of white matter fibre orientation on MR signal phase and decay. NMR Biomed. 2011; 24:246–252. [PubMed: 21404336]

Drayer B, Burger P, Darwin R, Riederer S, Herfkens R, Johnson GA. MRI of brain iron. AJR Am J Roentgenol. 1986; 147:103–110. [PubMed: 3487201]

Duyn JH, van Gelderen P, Li TQ, de Zwart JA, Koretsky AP, Fukunaga M. High-field MRI of brain cortical substructure based on signal phase. Proc Natl Acad Sci U S A. 2007; 104:11796–11801. [PubMed: 17586684]

Ferris CF, Snowdon CT, King JA, Duong TQ, Ziegler TE, Ugurbil K, Ludwig R, Schultz-Darken NJ, Wu Z, Olson DP, Sullivan JM Jr, Tannenbaum PL, Vaughan JT. Functional imaging of brain activity in conscious monkeys responding to sexually arousing cues. Neuroreport. 2001; 12:2231–2236. [PubMed: 11447340]

Fukunaga M, Li TQ, van Gelderen P, de Zwart JA, Shmueli K, Yao B, Lee J, Maric D, Aronova MA, Zhang G, Leapman RD, Schenck JF, Merkle H, Duyn JH. Layer-specific variation of iron content in cerebral cortex as a source of MRI contrast. Proc Natl Acad Sci U S A. 2010; 107:3834–3839. [PubMed: 20133720]

Gelman N, Gorell JM, Barker PB, Savage RM, Spickler EM, Windham JP, Knight RA. MR imaging of human brain at 3.0 T: preliminary report on transverse relaxation rates and relation to estimated iron content. Radiology. 1999; 210:759–767. [PubMed: 10207479]

Guilfoyle DN, Dyakin VV, O'Shea J, Pell GS, Helpern JA. Quantitative measurements of proton spin-lattice (T1) and spin-spin (T2) relaxation times in the mouse brain at 7.0 T. Magn Reson Med. 2003; 49:576–580. [PubMed: 12594763]

Haacke EM, Cheng NY, House MJ, Liu Q, Neelavalli J, Ogg RJ, Khan A, Ayaz M, Kirsch W, Obenaus A. Imaging iron stores in the brain using magnetic resonance imaging. Magn Reson Imaging. 2005; 23:1–25. [PubMed: 15733784]

He X, Yablonskiy DA. Biophysical mechanisms of phase contrast in gradient echo MRI. Proc Natl Acad Sci U S A. 2009; 106:13558–13563. [PubMed: 19628691]

He X, Zhu M, Yablonskiy DA. Validation of oxygen extraction fraction measurement by qBOLD technique. Magn Reson Med. 2008; 60:882–888. [PubMed: 18816808]

Hikishima K, Quallo MM, Komaki Y, Yamada M, Kawai K, Momoshima S, Okano HJ, Sasaki E, Tamaoki N, Lemon RN, Iriki A, Okano H. Population-averaged standard template brain atlas for the common marmoset (Callithrix jacchus). Neuroimage. 2011; 54:2741–2749. [PubMed: 21044887]

Hwang D, Kim DH, Du YP. In vivo multi-slice mapping of myelin water content using T2* decay. Neuroimage. 2010; 52:198–204. [PubMed: 20398770]

Kap YS, Laman JD, t Hart BA. Experimental autoimmune encephalomyelitis in the common marmoset, a bridge between rodent EAE and multiple sclerosis for immunotherapy development. J Neuroimmune Pharmacol. 2010; 5:220–230. [PubMed: 19826959]

Lee J, Shmueli K, Fukunaga M, van Gelderen P, Merkle H, Silva AC, Duyn JH. Sensitivity of MRI resonance frequency to the orientation of brain tissue microstructure. Proc Natl Acad Sci U S A. 2010; 107:5130–5135. [PubMed: 20202922]

Lee J, Van Gelderen P, Kuo L, Merkle H, Silva AC, Duyn J. T2*-based fiber orientation mapping. Neuroimage. 2011a; 57:225–234. [PubMed: 21549203]

Lee, J.; Yao, B.; Palumbo, S.; Shmueli, K.; van Gelderen, P.; Bosetti, F.; Silva, AC.; Duyn, J. Ultra-High Field Systems and Applications: 7T and beyond. Alberta, Canada: 2011b. MRI T2* relaxation and Frequency Contrast Changes in Cuprizone-Fed Mice.

Li TQ, van Gelderen P, Merkle H, Talagala L, Koretsky AP, Duyn J. Extensive heterogeneity in white matter intensity in high-resolution T2*-weighted MRI of the human brain at 7.0 T. Neuroimage. 2006; 32:1032–1040. [PubMed: 16854600]

Li TQ, Yao B, van Gelderen P, Merkle H, Dodd S, Talagala L, Koretsky AP, Duyn J. Characterization of T(2)* heterogeneity in human brain white matter. Magn Reson Med. 2009; 62:1652–1657. [PubMed: 19859939]

Liu C. Susceptibility tensor imaging. Magn Reson Med. 2010; 63:1471–1477. [PubMed: 20512849]

Liu C, Li W, Johnson GA, Wu B. High-field (9.4T) MRI of brain dysmyelination by quantitative mapping of magnetic susceptibility. Neuroimage. 2011a; 56:930–938. [PubMed: 21320606]

Liu JV, Bock NA, Silva AC. Rapid high-resolution three-dimensional mapping of T1 and age-dependent variations in the non-human primate brain using magnetization-prepared rapid gradient-echo (MPRAGE) sequence. Neuroimage. 2011b; 56:1154–1163. [PubMed: 21376814]

Lucas BC, Bogovic JA, Carass A, Bazin PL, Prince JL, Pham DL, Landman BA. The Java Image Science Toolkit (JIST) for rapid prototyping and publishing of neuroimaging software. Neuroinformatics. 2010; 8:5–17. [PubMed: 20077162]

Newman JD, Kenkel WM, Aronoff EC, Bock NA, Zametkin MR, Silva AC. A combined histological and MRI brain atlas of the common marmoset monkey, Callithrix jacchus. Brain Res Rev. 2009; 62:1–18. [PubMed: 19744521]

Ogawa S, Lee TM, Kay AR, Tank DW. Brain magnetic resonance imaging with contrast dependent on blood oxygenation. Proc Natl Acad Sci U S A. 1990; 87:9868–9872. [PubMed: 2124706]

Oros-Peusquens AM, Laurila M, Shah NJ. Magnetic field dependence of the distribution of NMR relaxation times in the living human brain. MAGMA. 2008; 21:131–147. [PubMed: 18338191]

Reichenbach JR, Venkatesan R, Schillinger DJ, Kido DK, Haacke EM. Small vessels in the human brain: MR venography with deoxyhemoglobin as an intrinsic contrast agent. Radiology. 1997; 204:272–277. [PubMed: 9205259]

Sati P, Cross AH, Luo J, Hildebolt CF, Yablonskiy DA. In vivo quantitative evaluation of brain tissue damage in multiple sclerosis using gradient echo plural contrast imaging technique. Neuroimage. 2010; 51:1089–1097. [PubMed: 20338247]

Schäfer, A.; Bowtell, R.; Turner, R. Orientation dependence of grey/whitte matter contrast in ultra high fields. 17th Annual Meeting of the International Society of Magnetic Resonance in Medicine; Honolulu, Hawaii. 2009.

Scharf J, Brauherr E, Forsting M, Sartor K. Significance of haemorrhagic lacunes on MRI in patients with hypertensive cerebrovascular disease and intracerebral haemorrhage. Neuroradiology. 1994; 36:504–508. [PubMed: 7845571]

Stanisz GJ, Odrobina EE, Pun J, Escaravage M, Graham SJ, Bronskill MJ, Henkelman RM. T1, T2 relaxation and magnetization transfer in tissue at 3T. Magn Reson Med. 2005; 54:507–512. [PubMed: 16086319]

Stefanovic B, Sled JG, Pike GB. Quantitative T2 in the occipital lobe: the role of the CPMG refocusing rate. J Magn Reson Imaging. 2003; 18:302–309. [PubMed: 12938124]

Wansapura JP, Holland SK, Dunn RS, Ball WS Jr. NMR relaxation times in the human brain at 3.0 tesla. J Magn Reson Imaging. 1999; 9:531–538. [PubMed: 10232510]

Wiggins, C.; Gudmundsdottir, V.; Le Bihan, D.; Lebon, V.; Chaumeil, M. Orientation Dependence of White Matter T2* contrast at 7T: A Direct Demonstration. 16th Annual Meeting the International Society of Magnetic Resonance in Medicine; Toronto, Canada. 2008.

Wiggins, G.; Wiggins, C.; Zhang, B.; Brown, R.; Stoeckel, B.; Sodickson, DK. Exploring Orientation Dependence of T2* in White Matter by Extreme Rotation of the Human Head at 7 Tesla. 19th Annual Meeting of the International Society of Magnetic Resonance in Medicine; Montreal, Canada. 2011.

Yablonskiy DA. Quantitation of intrinsic magnetic susceptibility-related effects in a tissue matrix. Phantom study. Magn Reson Med. 1998; 39:417–428. [PubMed: 9498598]

Yablonskiy DA, Haacke EM. Theory of NMR signal behavior in magnetically inhomogeneous tissues: the static dephasing regime. Magn Reson Med. 1994; 32:749–763. [PubMed: 7869897]

Yamada M, Momoshima S, Masutani Y, Fujiyoshi K, Abe O, Nakamura M, Aoki S, Tamaoki N, Okano H. Diffusion-tensor neuronal fiber tractography and manganese-enhanced MR imaging of primate visual pathway in the common marmoset: preliminary results. Radiology. 2008; 249:855–864. [PubMed: 19011185]

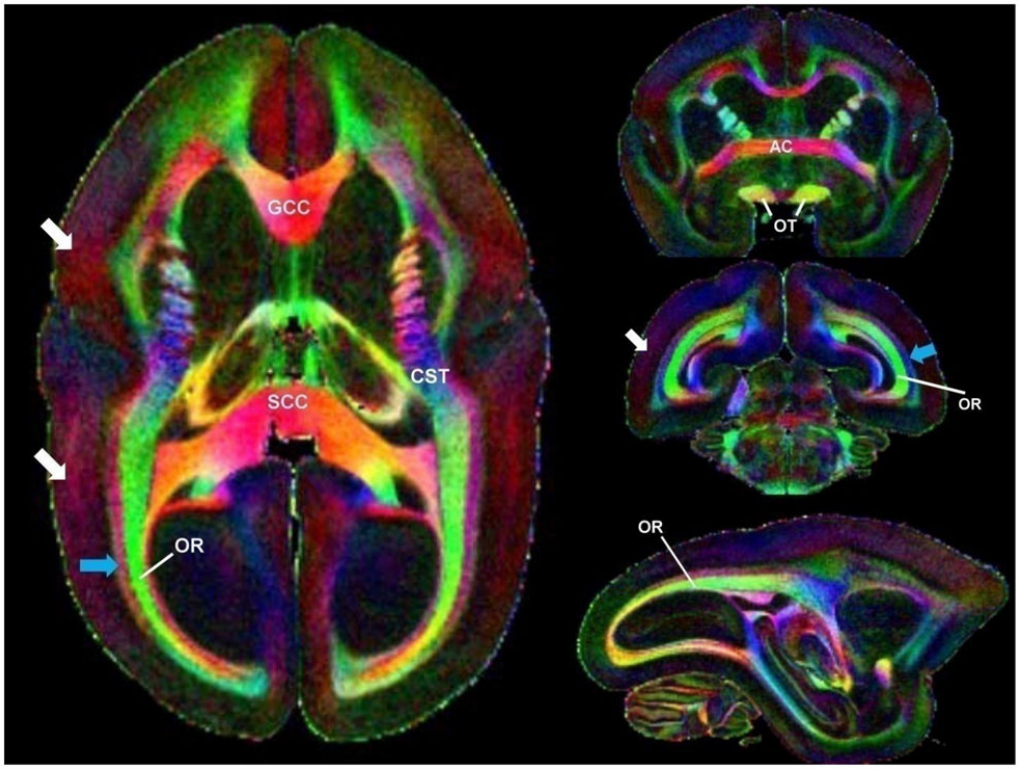

Figure 1.
Color-encoded fractional anisotropy maps acquired ex vivo with a nominal voxel size of 150 μm^3. The image on the left corresponds to an axial view, the top and middle images on the right to coronal views (from anterior to posterior), and the bottom image to a sagittal view. Red, green, and blue colors encode fiber bundles along the right-left, anterior-posterior, and head-foot directions, respectively. Note the optic radiations (OR) and the adjacent fibers that run orthogonally to them (blue arrow). Note also that the cortex has areas with increased fractional anisotropy (white arrows). Abbreviations: GCC, genu of the corpus callosum; SCC, splenium of the corpus callosum; CST, corticospinal tract; AC, anterior commissure.

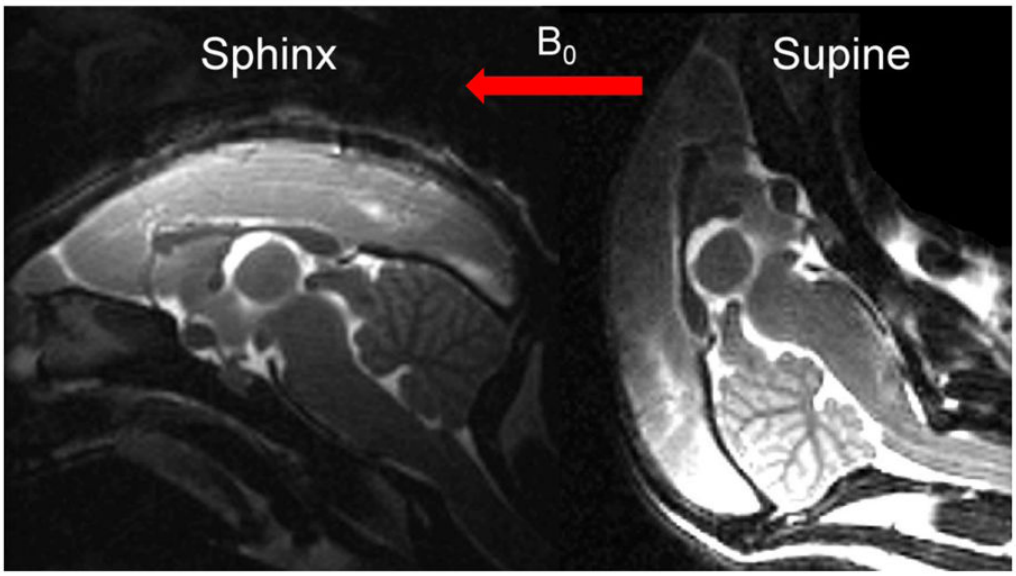

Figure 2.
Sagittal T_2-weighted spin-echo localizer images acquired in vivo. The left and right images show the marmoset head orientation in the sphinx position and the supine position, respectively. The red arrow shows the direction of the main magnetic field (B_0) in both experiments.

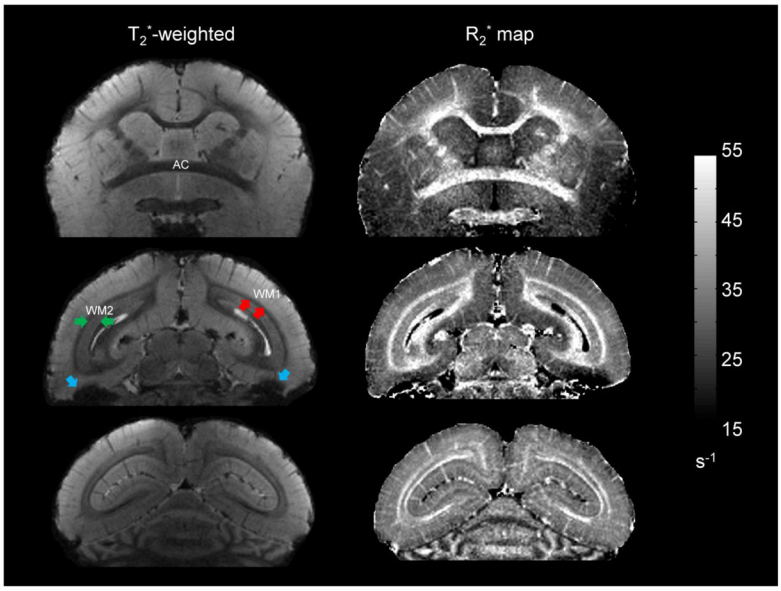

Figure 3.

Different coronal slices from the same monkey acquired in sphinx position. The left column shows the magnitude image averaged over the three longest echoes (TE = 24.5, 31.5, and 38.5 ms). The right column shows the corresponding R_2^* maps. Images are displayed from anterior (top) to posterior (bottom). The grayscale bar for R_2^* relaxation rate is given in s^{-1}. The optic radiations, labeled as WM2 (green arrows), are adjacent to perpendicularly oriented fibers, labeled as WM1 (red arrows). Note the difference in T_2^* contrast and R_2^* values between these two adjacent fiber bundles. Note also the non-tissue-specific intensity variations observed in the inferior temporal lobes (blue arrows).

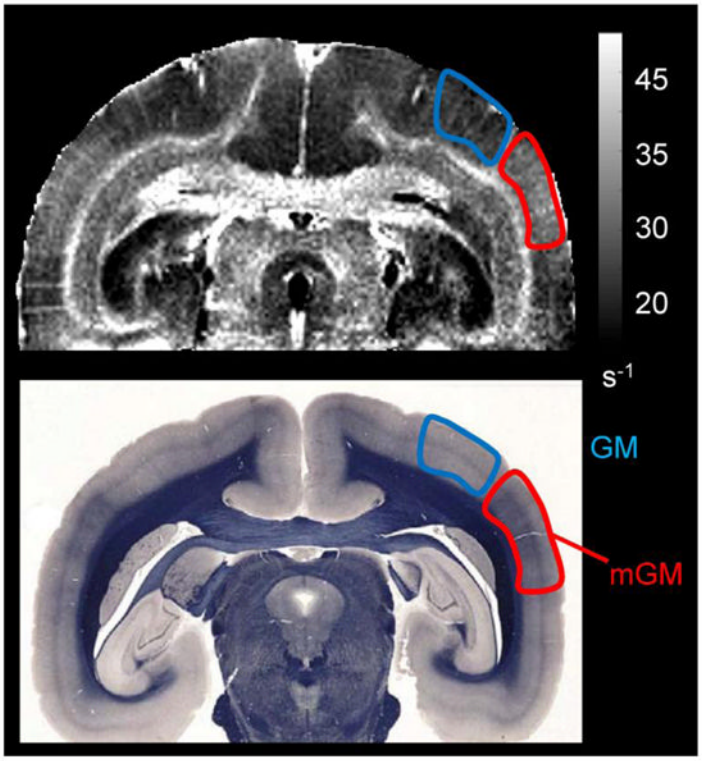

Figure 4.

The top image shows an R_2^* map acquired in vivo in the sphinx position. Grayscale bar for R_2^* relaxation rate is given in s^{-1}. The bottom image is a whole-mount section, stained for myelin using the Weil stain. In both images, the highly myelinated cortical area (middle temporal area MT) is outlined in red and labeled mGM, whereas the neighboring cortex, with lower myelin content, is outlined in blue and labeled GM. Note the excellent correspondence between the R_2^* relaxation rate map and myelin density.

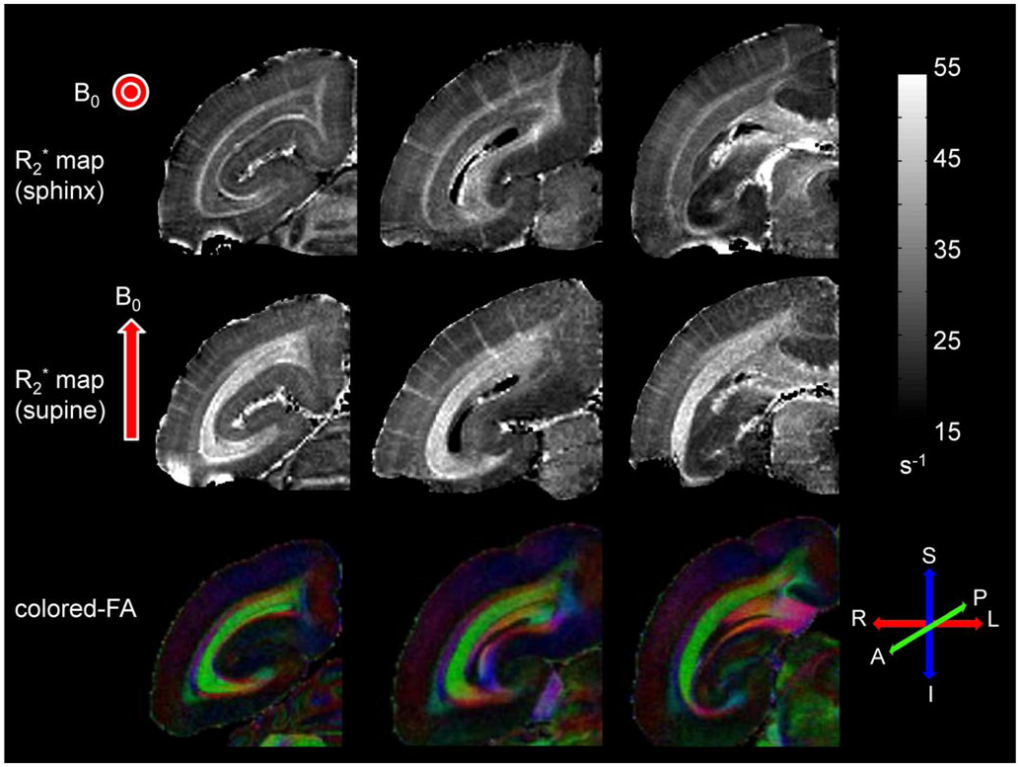

Figure 5.
The top row shows R_2^* maps from three coronal slices acquired in the sphinx position in vivo. The middle row shows R_2^* maps of the same slices acquired in the supine position, also in vivo. The bottom row shows the corresponding color-encoded fractional anisotropy maps acquired ex vivo from a different brain. Red arrows represent the orientation of the main field for each acquisition. Grayscale bar for R_2^* relaxation rate is given in s^{-1}. Red, green, and blue colors correspond to right-left, anterior-posterior, and superior-inferior orientations, respectively. Note that the contrast reverses in the white matter regions as the brain position is changed. Note also the excellent correspondence of the optic radiations on R_2^* maps acquired in the supine position and on the fractional anisotropy maps acquired ex vivo.

Table 1

Mean R_2^* ± SD (s^{-1}) in each marmoset, as well as the intermarmoset average (avg), calculated for different ROIs: GM, mGM, and selected WM regions (AC, GCC, SCC, WM1, and WM2). Values were obtained from MGRE data collected in the sphinx position. For one animal (#5), MGRE data were averaged four times (# avgs.=4) before R_2^* mapping. Abbreviations: GM, gray matter; mGM, myelinated gray matter; AC, anterior commissure; GCC, genu of the corpus callosum; SCC, splenium of the corpus callosum; WM, white matter.

Animal	# avgs.	GM	mGM	AC	GCC	SCC	WM1	WM2
1	1	25.1 ± 2.0	29.6 ± 2.9	39.6 ± 6.4	41.0 ± 6.8	41.5 ± 4.8	38.1 ± 4.5	30.0 ± 3.2
2	1	25.5 ± 2.4	29.9 ± 2.7	42.9 ± 6.8	43.8 ± 5.7	40.8 ± 5.5	40.1 ± 4.6	31.1 ± 2.5
3	1	24.7 ± 2.2	28.4 ± 2.9	34.3 ± 6.0	40.0 ± 7.0	42.4 ± 5.1	39.1 ± 5.1	29.9 ± 2.8
4	1	24.5 ± 2.3	29.2 ± 2.8	37.8 ± 4.6	43.5 ± 6.4	41.0 ± 4.9	38.1 ± 4.6	29.9 ± 2.7
5	4	23.3 ± 2.0	27.4 ± 2.5	N/A*	48.5 ± 9.1	41.0 ± 5.2	34.2 ± 3.9	27.7 ± 2.3
avg (mean[a] ± SD[b])		**24.6 ± 0.8**	**28.9 ± 1.0**	**38.6 ± 3.6**	**43.4 ± 3.3**	**41.3 ± 0.6**	**37.9 ± 2.2**	**29.7 ± 1.2**

[a] mean is the average of the individual means.

[b] SD is the standard deviation of the individual means.

* N/A (not available). For this animal (#5), the anterior commissure was not included in the field of view.

Table 2

Mean R_2^* ± SD (s^{-1}) of the two marmosets (#4 and #5) scanned in the two different head positions (sphinx and supine), as well as the intermarmoset average (avg), calculated for different ROIs: GM, mGM, and WM regions (WM1 and WM2). Note that WM2 corresponds to the optic radiations (OR) as explained in the text. For one animal (#5), MGRE data were averaged four times (NEX=4) before R_2^* mapping. The variation in R_2^* values (ΔR_2^*) between the two positions was calculated for each ROI. See Table 1 for abbreviations.

Position	Animal	# avgs.	GM	mGM	WM1	WM2 (OR)
Sphinx	4	1	24.5 ± 2.3	29.2 ± 2.8	38.1 ± 4.6	29.9 ± 2.7
	5	4	23.3 ± 2.0	27.4 ± 2.5	34.2 ± 3.9	27.7 ± 2.3
	avg (mean[a] ± SD[b])		**23.9 ± 0.8**	**28.3 ± 1.3**	**36.1 ± 2.7**	**28.8 ± 1.5**
Supine	4	1	22.1± 2.7	25.9 ± 2.9	29.8 ± 5.0	40.9 ± 5.7
	5	4	24.3 ± 2.6	29.6 ± 3.1	32.4 ± 4.0	46.2 ± 5.2
	avg (mean[a] ± SD[b])		**23.2 ± 1.5**	**27.7 ± 2.6**	**31.1 ± 1.8**	**43.5 ± 3.7**
ΔR2* (mean[c] ± SD[d])			**−0.7 ± 1.7**	**−0.6 ± 2.9**	**−5.0 ± 3.2**	**+14.7 ± 4.0**

[a] mean is the average of the individual means.

[b] SD is the standard deviation of the individual means.

[c] mean of ΔR_2^* is calculated by subtracting the mean[a] of the sphinx position to the mean[a] of the supine position.

[d] SD of ΔR_2^* is calculated using the square root of the sum of the squared standard deviations (SD[b]) of sphinx and supine positions.